

Northumbria Research Link

Citation: Mikhaylov, Roman, Martin, Mercedes Stringer, Dumcius, Povilas, Wang, Hanlin, Wu, Fangda, Zhang, Xiaoyan, Alghamdi, Fahad, Akhimien, Victory, Sun, Chao, Clayton, Aled, Fu, Richard, Ye, Lin, Dong, Zhiqiang and Yang, Xin (2021) A Reconfigurable and Portable Acoustofluidic System Based on Flexible Printed Circuit Board for the Manipulation of Microspheres. *Journal of Micromechanics and Microengineering*, 31 (7). 074003. ISSN 0960-1317

Published by: IOP Publishing

URL: <https://doi.org/10.1088/1361-6439/ac0515> <<https://doi.org/10.1088/1361-6439/ac0515>>

This version was downloaded from Northumbria Research Link:
<http://nrl.northumbria.ac.uk/id/eprint/46360/>

Northumbria University has developed Northumbria Research Link (NRL) to enable users to access the University's research output. Copyright © and moral rights for items on NRL are retained by the individual author(s) and/or other copyright owners. Single copies of full items can be reproduced, displayed or performed, and given to third parties in any format or medium for personal research or study, educational, or not-for-profit purposes without prior permission or charge, provided the authors, title and full bibliographic details are given, as well as a hyperlink and/or URL to the original metadata page. The content must not be changed in any way. Full items must not be sold commercially in any format or medium without formal permission of the copyright holder. The full policy is available online: <http://nrl.northumbria.ac.uk/policies.html>

This document may differ from the final, published version of the research and has been made available online in accordance with publisher policies. To read and/or cite from the published version of the research, please visit the publisher's website (a subscription may be required.)

1 **A Reconfigurable and Portable Acoustofluidic System Based on Flexible**
2 **Printed Circuit Board for the Manipulation of Microspheres**

3 Roman Mikhaylov¹, Mercedes Stringer Martin¹, Povilas Dumcius¹, Hanlin Wang¹, Fangda Wu¹,
4 Xiaoyan Zhang², Fahad Alghamdi¹, Victory Akhimien¹, Chao Sun³, Aled Clayton⁴, Yongqing Fu⁵,
5 Lin Ye⁶, Zhiqiang Dong⁷, and Xin Yang¹

6 ¹ Department of Electrical and Electronic Engineering, School of Engineering, Cardiff
7 University, Cardiff CF24 3AA, UK

8 ² International Joint Laboratory of Biomedicine and Engineering, Huazhong Agricultural
9 University and Cardiff University, Wuhan, Hubei, 430070, China

10 ³ School of Life Sciences, Northwestern Polytechnical University, 710072, P.R. China

11 ⁴ Tissue Micro-Environment Group, Division of Cancer & Genetics, School of Medicine,
12 Cardiff University, Cardiff CF14 4XN, UK

13 ⁵ Faculty of Engineering and Environment, Northumbria University, Newcastle Upon Tyne,
14 Newcastle NE1 8ST, UK

15 ⁶ Cardiff China Medical Research Collaborative, Division of Cancer & Genetics, Cardiff
16 University School of Medicine, Cardiff, CF14 4XN, UK

17 ⁷ College of Biomedicine and Health, College of Life Science and Technology, Huazhong
18 Agricultural University, Wuhan, Hubei, 430070, China

19
20
21
22
23
24
25
26
27
28
29
30
31
32
33
34
35
36
37
38
39
40
41
42
43
44

Corresponding author: Xin Yang

45 **Abstract**

46 Acoustofluidic devices based on surface acoustic waves (SAWs) have been widely applied in
47 biomedical research for the manipulation and separation of cells. In this work, we develop an
48 accessible manufacturing process to fabricate an acoustofluidic device consisting of a SAW
49 interdigital transducer (IDT) and a polydimethylsiloxane (PDMS) microchannel. The IDT is
50 manufactured using a flexible printed circuit board (FPCB) pre-patterned with interdigital
51 electrodes (IDEs) that is mechanically coupled with a piezoelectric substrate. A new microchannel
52 moulding technique is realised by 3D printing on glass slides and is demonstrated by constructing
53 the microchannel for the acoustofluidic device. The flexible clamping mechanism, used to
54 construct the device, allows the reconfigurable binding between the IDT and the microchannel.
55 This unique construction makes the acoustofluidic device capable of adjusting the angle between
56 the microchannel and the SAW propagation, without refabrication, via either rotating the IDT or
57 the microchannel. The angle adjustment is demonstrated by setting the polystyrene microsphere
58 aggregation angle to -5° , 0° , 6° , and 15° . Acoustic energy density measurements demonstrate the
59 velocity of microsphere aggregation in the device can be accurately controlled by the input power.
60 The manufacturing process has the advantages of reconfigurability and rapid-prototyping to
61 facilitate preparing acoustofluidic devices for wider applications.

62 **Introduction**

63 Acoustofluidic devices have attracted great interest in label-free manipulations of micro-¹ and
64 nano- particles² owing to their considerable biocompatibility and precision. They have been
65 demonstrated in biomedical applications for separation (exosomes³⁻⁵, tumour⁶, and inflammatory⁷
66 cells), manipulation (cell interaction⁸, single cells⁹, and *Caenorhabditis elegans*¹⁰), and stimulation
67 of cells¹¹.

68 Surface acoustic wave (SAW) devices are almost independent from the microchannel material
69 in terms of acoustic properties compared to bulk acoustic wave devices¹². This feature makes them
70 easy to fabricate for high-frequency applications (MHz-GHz)^{3,13} and integrate with other systems,
71 such as microfluidics. SAW devices are conventionally fabricated by patterning interdigital
72 transducers (IDTs) on a piezoelectric substrate¹⁴, which convert radio frequency (RF) signals into
73 SAWs propagating on the surface of the substrate. When the SAW meets a liquid medium, it
74 diffracts into the medium and generates a time-averaged pressure distribution that can be utilised
75 to precisely manipulate micro-objects¹⁵. Standing SAW (SSAW) devices, constructed by a pair of
76 opposite IDTs working on the same frequency, are primarily used in acoustofluidic applications¹⁶.
77 A great diversity of manipulation and actuation can be achieved by setting up the IDT structure to
78 create, for example, tilted-angle SSAW devices^{17,18} and 2D- and 3D-patterning tweezers^{8,19-21}.
79 However, IDTs manufactured through conventional techniques, such as photolithography, are
80 permanently patterned on the piezoelectric substrate. Polydimethylsiloxane (PDMS)
81 microchannels, used to accommodate biological samples in acoustofluidic systems, also use the
82 photolithography process involving cleanroom facilities. Thus, acoustofluidic devices capable of
83 manufacturing and reconfiguring in general laboratories, using off-the-shelf components, are
84 highly desired.

85 A new fabrication technique, developed by our group, has successfully fabricated the IDTs
86 without the use of a cleanroom for the manipulation of microparticles and cancer cells²². The IDTs
87 were manufactured by mechanically clamping a rigid printed circuit board (PCB) pre-patterned
88 with interdigital electrodes (IDEs) onto a piezoelectric substrate. This technique has been

89 benchmarked against a device made by conventional photolithography in terms of frequency
90 response, droplet transportation, and cell manipulation. The PCB-based IDT has the advantage of
91 replacing piezoelectric substrates by simply disassembling the mechanically clamped structure,
92 with no need to remanufacture the IDT. Another IDT made by flexible PCB (FPCB) pre-patterned
93 with IDEs demonstrated similar performance with advantages of dynamic flexing, less weight, and
94 better heat dissipation²³.

95 A development process with low requirement on facilities and operation of the device using a
96 portable control unit can better support broadening the use of the acoustofluidic devices. Herein,
97 we present a novel development technique for both the IDTs and the microchannel, we call it
98 Versatile Acoustofluidic Device (VAD). We also demonstrate the rapid-prototyping and
99 reconfigurability of VAD for precise manipulation of micro-objects.

100 **Methods and Materials**

101 **FPCBs**

102 The FPCB pre-patterned with IDEs, used in the VAD, was externally manufactured
103 (circuitfly.com) using a standard PCB manufacturing process. The IDEs were made of metal
104 bilayers (Au/Ni, 30 nm/2 μm) patterned on a 70 μm thick polyester laminate. The IDEs consist of
105 40 pairs of 10 mm long finger electrodes and have a centre-to-centre finger pitch of 200 μm as
106 shown in Fig. 1A. The ratio between the finger spacing and finger width is 1:1. A 128° Y-cut 3-
107 inch lithium niobate (LiNbO_3) was used as the piezoelectric substrate. The VAD had a Rayleigh
108 mode frequency of ~ 19.9 MHz and a 200 μm wavelength. Two coaxial cables were soldered to
109 the buspads of each FPCB IDEs. Matching networks (MNs) based on an LC circuit are used (Fig.
110 1B), which are essential in reducing the impedance mismatching between the VAD and the driving
111 power amplifiers^{22,23}.

112

113 **Clamping Mechanism**

114 The VAD required a mechanical jig to hold the main components together, including the FPCB
115 IDEs and LiNbO_3 substrate. As shown in Fig. 1C, the VAD uses a simple clamping mechanism
116 and consists of the following stacking order from the bottom to the top: heatsink (supports the
117 entire device and dissipates heat), temperature sensors (measure the IDT temperature), LiNbO_3
118 (produces SAWs), FPCB IDEs (convert RF to SAWs), silicon pads (evenly distribute the clamping
119 force), localised pressers (apply the clamping force), force-sensitive resistors (FSRs) (measure the
120 clamping force), FSR roofs (hold and press the FSRs), M5 screws (generate the clamping force)
121 and main holders (hold the whole structure onto the heatsink). Another structure, which consists
122 of an acrylic presser and a microchannel presser, is developed to hold the microchannel between
123 the two IDTs. The FSR roofs, localised pressers, microchannel pressers, and main holders were all
124 3D printed using a 0.4 mm nozzle and polylactic acid (PLA) filaments.

125

126 **The VAD Assembly**

127 The FPCB IDEs, microchannel and LiNbO_3 substrate were thoroughly cleaned using isopropyl
128 alcohol and de-ionised (DI) water, dried using a compressed air duster and checked under the
129 microscope to ensure that no fibres or dust particles were present on the parts before the final
130 assembly. All the individual components, shown in Fig. 1C, are placed on the LiNbO_3 which is
131 mounted on the heatsink. A clamping force is created by fastening the two M5 screws on top of
132 the localised pressers. A vector network analyser (VNA) is used to monitor the reflection

133 coefficient (S_{11}) and to confirm when the contact resistance is overcome and an optimal clamping
134 force is achieved^{22,23}. Fig. 1D shows the final assembled VAD with a portable control unit and an
135 inset to demonstrate the full assembly including the microchannel on the heatsink.
136

137 **Microchannels**

138 The use of a glass-bottom 3D printed mould to prepare the microchannels stands as a novelty
139 for microchannel manufacturing, with the development flow illustrated in Fig. 2A. (1) A glass
140 slide (76 mm (W) × 26 mm (L)) is placed on the 3D printer table and held in place using masking
141 tape. A compensatory offset is applied by using a “Z offset setting” plugin in the 3D printer
142 software. Glass slides with various thicknesses can be used as the glass-bottom of the mould by
143 adjusting the offset setting. The 3D printed mould, designed in Solidworks, is directly printed on
144 the glass slide, (2) removed from the 3D printer table after completion and left to cool. (3) The
145 glass-bottom 3D printed mould is then placed in a plastic petri dish and filled with PDMS (Sylgard
146 184, Farnell UK), which is prepared according to the manufacturer’s protocol. The dish is placed
147 onto a hot plate (SD160, Colepalmer) at a temperature of 45 °C to cure for 24 hours, which is
148 below the 60 °C melting temperature of the PLA. (4) The set PDMS is removed from the mould,
149 (5) the outer perimeter of the channel is cut and (6) a premade acrylic presser, with the dimensions
150 of 47 mm (L) × 15 mm (W) × 3 mm (H), is placed on top of the microchannel. (7) The
151 microchannel is then bolted onto the pre-assembled VAD using a microchannel presser (Fig. 2B).
152 (8) The M5 nuts on the far edges of the microchannel presser are fastened until resistance is felt
153 and (9) finally the M3 screws are screwed in to ensure even distribution of the pressing force.

154 The walls of the microchannel presser (Fig. 2A, step 9 and Fig. 2B) are created to resist
155 excessive force and prevent it from overbending. These help to keep the force evenly distributed
156 across the microchannel and not to over compress it. To further prevent deformation, the ratio
157 between the PDMS and the microchannel height was 55:1.

158 Two examples of the glass-bottom 3D printed moulds are shown in Fig. 2C, which are single
159 inlet/outlet and 3-inlet-2-outlet structures, respectively. Five 3D printed moulds were printed on
160 the same glass slide and measured using a microscope to determine the repeatability of the print.
161

162 **Control Unit**

163 To increase the portability of the acoustofluidic system and facilitate on-demand use of the
164 VAD, a portable control unit that includes a waveform generator, a power amplifier, a
165 microcontroller, sensors, a display, and a power supply is developed (Fig. 3).
166

167 **Coating and Sample Preparation**

168 The microchannels were all coated with 1% (w/w) bovine serum albumin solution for 10 min
169 and then flushed with DI water. For the microsphere test, 10 µm polystyrene microspheres (Sigma
170 Aldrich) were used and suspended in a 23% (v/v) glycerol and phosphate-buffered saline solution.
171 The microsphere suspension was injected into the microchannels through a syringe.
172

173 **IDT Alignment Setup and Analysis**

174 The formation of SSAW relies on the alignment of the two IDTs, which can be reflected by the
175 device’s insertion loss (S_{21}). The smaller the insertion loss, the better the SAW transmission from
176 one IDT to another. Thus, one can effectively use the VNA to estimate the IDT alignment. This is
177 demonstrated by connecting two IDTs to the VNA as a two-port network, as shown in Fig 4. The
178 test keeps one of the IDTs unmoved, as the receiving IDT, while rotating the other IDT, as the

179 transmitting IDT. The S_{11} of the transmitting IDT is measured during this procedure to monitor
180 how it changes with the rotation. Top view images of the transmitting IDT at different orientations
181 were captured by an overhead camera, which were then analysed using a customised MATLAB
182 code that extracted the angle between the two IDTs. Five reference angles, 17°, 11°, 6°, 2°, and
183 0°, were determined for the S_{21} readings, which were selected by finding the most observable
184 change in the S_{21} .

185

186 **Acoustic Energy Density Analysis**

187 To characterise the acoustic energy density inside the VAD, a MATLAB code adapted from
188 Barnkob et al²⁴ was applied to analyse the trajectory of microspheres. In short, image frames
189 extracted from microscope-captured movies, during the microsphere aggregation process, were
190 analysed for pixel intensity near the pressure node (PN) line. The last frame of each movie was
191 used as the maximum intensity frame. The normalised intensity and the relative intensity of each
192 middle-process frames were then calculated and fit into an expression using a fitting parameter.

193 **Results and Discussion**

194 **IDT Alignment**

195 Compared to cleanroom made SSAW devices, the VAD depended on the manual alignment of
196 the two IDTs to produce an accurate SSAW and form an even distribution of PN and pressure anti-
197 node lines. The S_{21} peak can be used to establish the angle of the IDTs, where the 0° angle achieves
198 the maximum S_{21} peak as shown in Fig. 5A. The S_{11} of the transmitting IDT shows a dip of -28 dB
199 when the two IDTs are in parallel (Fig. 5B), which is within an acceptable working range of
200 conventional SAW devices²⁵.

201

202 **Microchannel Characterisation**

203 Fig. 6A shows the average height and width of the 3D printed moulds, i.e. $102.8 \pm 11.4 \mu\text{m}$
204 (Mean \pm SD) and $451.4 \pm 42.6 \mu\text{m}$ (Mean \pm SD), respectively. Of which a 500 μm wide 3D printed
205 mould is used to produce the microchannel for the following tests (Fig. 6B). The bonding strength
206 of the assembled microchannel met the high throughput requirement by flushing a sample at a flow
207 rate of up to 6 mL/min²⁶.

208

209 **Acoustic Energy Density within the VAD**

210 The acoustic energy density of the VAD at 0° is registered at 15, 20 and 27 dBm input power,
211 as the results shown in Figs. 7A-7C, respectively. The time lapse required for 99% of microspheres
212 to aggregate on the PN line is ~ 1.9 , ~ 0.6 , and ~ 0.3 sec for the three input powers. The average
213 acoustic energy density of the powers is shown in Fig. 7D, which indicates that the acoustic
214 radiation force exerted on the microspheres can be fully controlled by tuning the input power.

215

216 **Rotating the IDTs to Adjust the Tilted-Angle**

217 The VAD can offer reconfigurable tilted-angles (angle between the PN lines and the
218 microchannel) without the need of fabricating new devices. The optimal tilted-angle degree in cell
219 separation depends on the sample flow rate, where a high tilted-angle is optimal for the flow rate
220 of 25 $\mu\text{L}/\text{min}$ and a low tilted-angle for 50-125 $\mu\text{L}/\text{min}$ ⁶. The ability of VAD to vary the tilted-
221 angle can potentially save considerable manufacturing effort and cost in reconfiguring devices for
222 versatile and flexible applications. By simply rotating one of the IDTs, we manage to configure

223 the PN lines orientation into two tilted-angles, 0° and 6° , illustrated by the microsphere aggregation
224 shown in Figs. 8A and 8B, respectively. The results demonstrate the ability of the VAD in rapid
225 reconfiguration of the tilted-angle to tackle different applications.
226

227 **Visually Guided Assembly of the VAD**

228 The VAD is tested for whether visually aligning the two opposite IDTs by eye can achieve
229 similar performance as the VNA guided assembly. The VAD is assembled visually using the FSRs
230 readings as reference. The alignment quality, represented by the S_{21} , is shown in Fig. 9A.
231 Comparing with the VNA guided alignments (blue curve), the visually guided alignments (orange
232 curve) present a smaller S_{21} . Fig. 9B shows the acoustic energy density is slightly higher in the
233 visually guided assembly. This could be because the distance between the opposing IDTs may
234 have been reduced during the visual experiments⁶. Since the IDTs are pushed further forward to
235 expose their front edge and allow them to be easily visually aligned.

236 In addition, we collected the microsphere aggregation image for the visually guided assembly,
237 as shown in Fig. 9C, which achieves a similar pattern as that in the VNA guided assembly (Fig.
238 8A). Overall, this confirms that the assembling process of the VAD can be achieved by the visual
239 alignment of the two IDTs without the use of the VNA.
240

241 **Rotating the Microchannel**

242 The unique construction of the VAD allows an alternative way to alter the tilted-angle by
243 rotating the microchannel clamped to the VAD. New microchannel pressers are printed with two
244 degrees including 15° and -5° to accommodate a wider microchannel as shown in Fig. 10A. These
245 pressers are utilised to clamp the microchannel and to create the respective inclinations for
246 aggregating the microspheres, as shown in Fig. 10B.

247 It is noted that the reconfiguration of the tilted-angles can be achieved by either rotating the
248 microchannel or the IDTs. It may be preferable to rotate the microchannel as it does not require to
249 rotate the IDT, which may potentially affect the frequency response of the VAD.

250 **Conclusion**

251 This paper introduced a novel technology to manufacture the SAW-based acoustofluidic
252 system, including both the SAW IDT and the PDMS microchannel, without the need of a
253 cleanroom facility. It was demonstrated that a pair of FPCB IDEs were mechanically coupled to
254 the piezoelectric substrate to produce SSAWs, under the guide of either eyes or the VNA. The
255 VAD offers great flexibility in resetting the tilted-angle between the IDTs and the microchannel,
256 resulting in rotatable PN lines inside the acoustofluidic device. The VAD can accomplish a rapid
257 acoustofluidic prototyping process as an alternative to the conventional cleanroom process.

258 **Acknowledgements**

259 The authors would gratefully acknowledge the financial support from EPSRC (EP/P002803/1,
260 EP/P018998/1), EPSRC IAA, Wellcome Trust, Global Challenges Research Fund (GCRF), the
261 Royal Society (IEC\NSFC\170142, IE161019), and the Natural Science Foundation of China
262 (NSFC) (Grant No. 51811530310).

263 **References**

- 264 1 Z. Tian, S. Yang, P.-H. Huang, Z. Wang, P. Zhang, Y. Gu, H. Bachman, C. Chen, M. Wu, Y.
265 Xie and T. J. Huang, Wave number–spiral acoustic tweezers for dynamic and reconfigurable
266 manipulation of particles and cells, *Science Advances*, 2019, **5**, eaau6062.
- 267 2 M. Wu, Z. Mao, K. Chen, H. Bachman, Y. Chen, J. Rufo, L. Ren, P. Li, L. Wang and T. J.
268 Huang, Acoustic Separation of Nanoparticles in Continuous Flow, *Advanced Functional*
269 *Materials*, 2017, **27**, 1606039.
- 270 3 M. Wu, Y. Ouyang, Z. Wang, R. Zhang, P.-H. Huang, C. Chen, H. Li, P. Li, D. Quinn, M. Dao,
271 S. Suresh, Y. Sadovsky and T. J. Huang, Isolation of exosomes from whole blood by integrating
272 acoustics and microfluidics, *Proc. Natl. Acad. Sci. U.S.A.*, 2017, **114**, 10584–10589.
- 273 4 M. Wu, C. Chen, Z. Wang, H. Bachman, Y. Ouyang, P.-H. Huang, Y. Sadovsky and T. J.
274 Huang, Separating extracellular vesicles and lipoproteins via acoustofluidics, *Lab Chip*, 2019,
275 **19**, 1174–1182.
- 276 5 Y. Gu, C. Chen, Z. Mao, H. Bachman, R. Becker, J. Rufo, Z. Wang, P. Zhang, J. Mai, S. Yang,
277 J. Zhang, S. Zhao, Y. Ouyang, D. T. W. Wong, Y. Sadovsky and T. J. Huang, Acoustofluidic
278 centrifuge for nanoparticle enrichment and separation, *Science Advances*, 2021, **7**, eabc0467.
- 279 6 P. Li, Z. Mao, Z. Peng, L. Zhou, Y. Chen, P.-H. Huang, C. I. Truica, J. J. Drabick, W. S. El-
280 Deiry, M. Dao, S. Suresh and T. J. Huang, Acoustic separation of circulating tumor cells, *PNAS*,
281 2015, **112**, 4970–4975.
- 282 7 S. Li, L. Ren, P.-H. Huang, X. Yao, R. A. Cuento, J. P. McCoy, C. E. Cameron, S. J. Levine
283 and T. J. Huang, Acoustofluidic Transfer of Inflammatory Cells from Human Sputum Samples,
284 *Analytical Chemistry*, 2016, **88**, 5655–5661.
- 285 8 F. Guo, P. Li, J. B. French, Z. Mao, H. Zhao, S. Li, N. Nama, J. R. Fick, S. J. Benkovic and T.
286 J. Huang, Controlling cell–cell interactions using surface acoustic waves, *PNAS*, 2015, **112**, 43–
287 48.
- 288 9 D. Ahmed, A. Ozcelik, N. Bojanala, N. Nama, A. Upadhyay, Y. Chen, W. Hanna-Rose and T.
289 J. Huang, Rotational manipulation of single cells and organisms using acoustic waves, *Nature*
290 *Communications*, 2016, **7**, 11085.
- 291 10 J. Zhang, S. Yang, C. Chen, J. H. Hartman, P.-H. Huang, L. Wang, Z. Tian, P. Zhang, D.
292 Faulkenberry, J. N. Meyer and T. J. Huang, Surface acoustic waves enable rotational
293 manipulation of *Caenorhabditis elegans*, *Lab Chip*, 2019, **19**, 984–992.
- 294 11 L. A. Ambattu, S. Ramesan, C. Dekiwadia, E. Hanssen, H. Li and L. Y. Yeo, High frequency
295 acoustic cell stimulation promotes exosome generation regulated by a calcium-dependent
296 mechanism, *Commun Biol*, 2020, **3**, 553.
- 297 12 K. Xu, C. P. Clark, B. L. Poe, J. A. Lounsbury, J. Nilsson, T. Laurell and J. P. Landers, Isolation
298 of a Low Number of Sperm Cells from Female DNA in a Glass–PDMS–Glass Microchip via
299 Bead-Assisted Acoustic Differential Extraction, *Anal. Chem.*, 2019, **91**, 2186–2191.
- 300 13 R. J. Shilton, M. Travagliati, F. Beltram and M. Cecchini, Nanoliter-Droplet Acoustic
301 Streaming via Ultra High Frequency Surface Acoustic Waves, *Advanced Materials*, 2014, **26**,
302 4941–4946.
- 303 14 Y. Ai, C. K. Sanders and B. L. Marrone, Separation of *Escherichia coli* Bacteria from Peripheral
304 Blood Mononuclear Cells Using Standing Surface Acoustic Waves, *Anal. Chem.*, 2013, **85**,
305 9126–9134.
- 306 15 N. Nama, R. Barnkob, Z. Mao, C. J. Kähler, F. Costanzo and T. J. Huang, Numerical study of
307 acoustophoretic motion of particles in a PDMS microchannel driven by surface acoustic waves,
308 *Lab Chip*, 2015, **15**, 2700–2709.

309 16A. Ozcelik, J. Rufo, F. Guo, Y. Gu, P. Li, J. Lata and T. J. Huang, Acoustic tweezers for the life
310 sciences, *Nature Methods*, 2018, **15**, 1021.

311 17G. Liu, F. He, Y. Li, H. Zhao, X. Li, H. Tang, Z. Li, Z. Yang and Y. Zhang, Effects of two
312 surface acoustic wave sorting chips on particles multi-level sorting, *Biomed Microdevices*,
313 2019, **21**, 59.

314 18K.-A. Hyun, H. Gwak, J. Lee, B. Kwak and H.-I. Jung, Salivary Exosome and Cell-Free DNA
315 for Cancer Detection, *Micromachines*, 2018, **9**, 340.

316 19Y. Wang, C. Han and D. Mei, Standing Surface Acoustic Wave-Assisted Fabrication of Region-
317 Selective Microstructures via User-Defined Waveguides, *Langmuir*, 2019, **35**, 11225–11231.

318 20F. Guo, Z. Mao, Y. Chen, Z. Xie, J. P. Lata, P. Li, L. Ren, J. Liu, J. Yang, M. Dao, S. Suresh
319 and T. J. Huang, Three-dimensional manipulation of single cells using surface acoustic waves,
320 *PNAS*, 2016, **113**, 1522–1527.

321 21T. D. Nguyen, V. T. Tran, Y. Q. Fu and H. Du, Patterning and manipulating microparticles into
322 a three-dimensional matrix using standing surface acoustic waves, *Appl. Phys. Lett.*, 2018, **112**,
323 213507.

324 22R. Mikhaylov, F. Wu, H. Wang, A. Clayton, C. Sun, Z. Xie, D. Liang, Y. Dong, F. Yuan, D.
325 Moschou, Z. Wu, M. H. Shen, J. Yang, Y. Fu, Z. Yang, C. Burton, R. J. Errington, M. Wiltshire
326 and X. Yang, Development and characterisation of acoustofluidic devices using detachable
327 electrodes made from PCB, *Lab Chip*, 2020, **20**, 1807–1814.

328 23C. Sun, R. Mikhaylov, Y. Fu, F. Wu, H. Wang, X. Yuan, Z. Xie, D. Liang, Z. Wu and X. Yang,
329 Flexible Printed Circuit Board as Novel Electrodes for Acoustofluidic Devices, *IEEE*
330 *Transactions on Electron Devices*, 2021, **68**, 393–398.

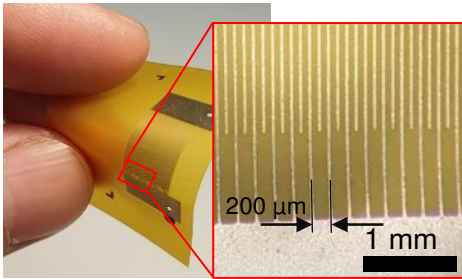
331 24R. Barnkob, I. Iranmanesh, M. Wiklund and H. Bruus, Measuring acoustic energy density in
332 microchannel acoustophoresis using a simple and rapid light-intensity method, *Lab on a Chip*,
333 2012, **12**, 2337–2344.

334 25F. Wu, M. H. Shen, J. Yang, H. Wang, R. Mikhaylov, A. Clayton, X. Qin, C. Sun, Z. Xie, M.
335 Cai, J. Wei, D. Liang, F. Yuan, Z. Wu, Y. Fu, Z. Yang, X. Sun, L. Tian and X. Yang, An
336 Enhanced Tilted-Angle Acoustofluidic Chip for Cancer Cell Manipulation, *IEEE Electron*
337 *Device Letters*, 2021, **42**, 577–580.

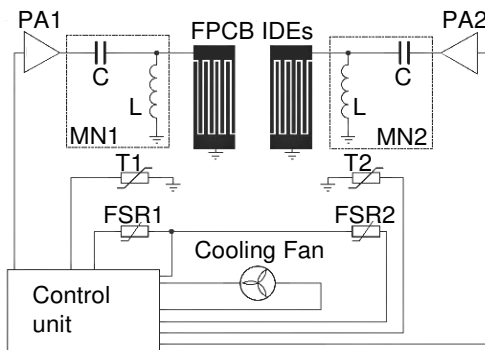
338 26Y. Chen, M. Wu, L. Ren, J. Liu, P. H. Whitley, L. Wang and T. J. Huang, High-throughput
339 acoustic separation of platelets from whole blood, *Lab Chip*, 2016, **16**, 3466–3472.

340

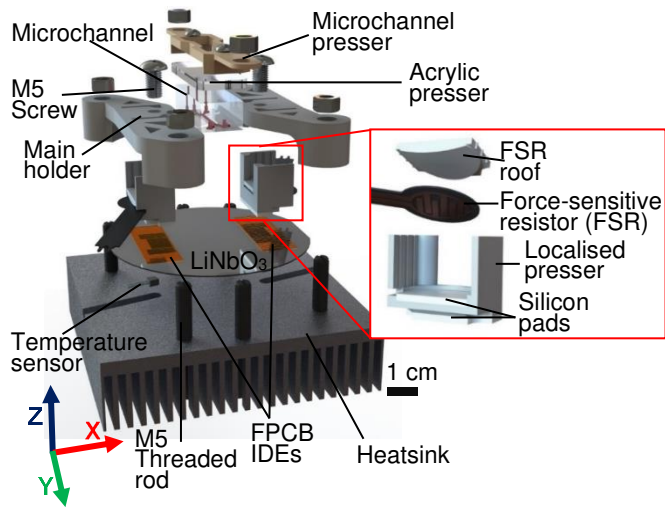
341 **FIGURE LIST**



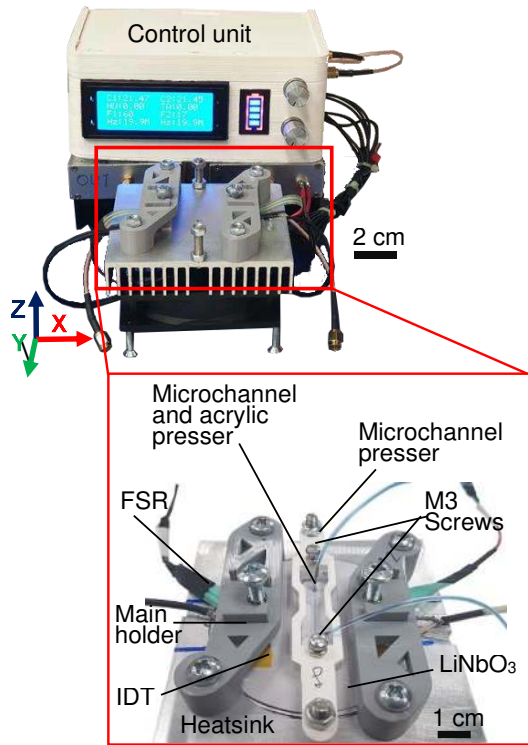
342 (A)



343 (B)

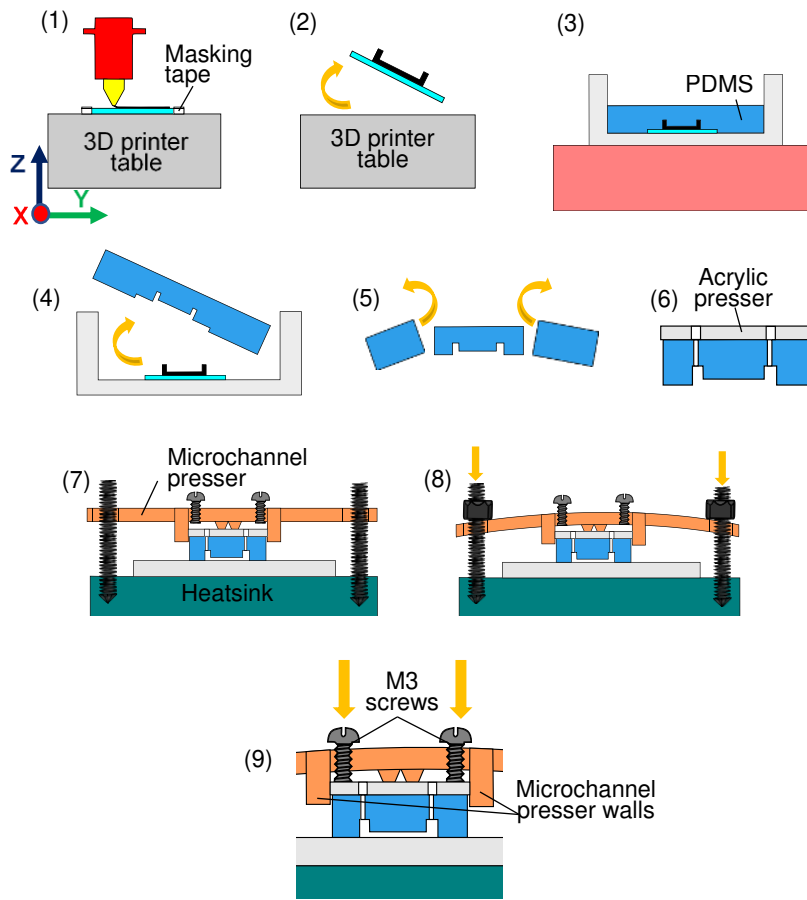


344 (C)

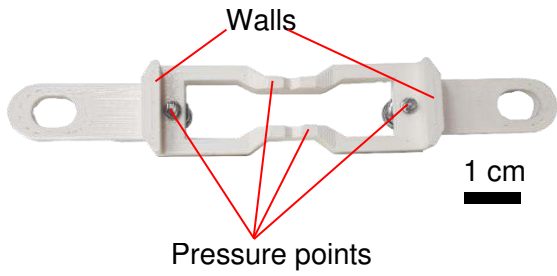


345 (D)

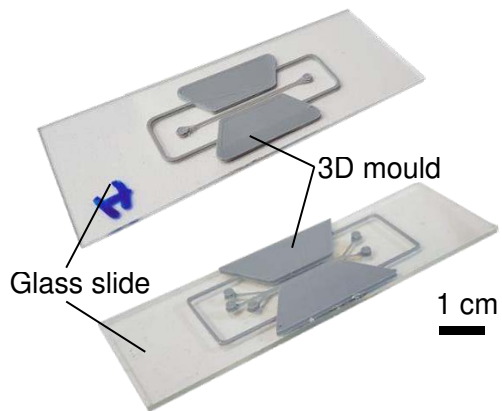
346 **Figure 1.** (A) Real-life flexible printed circuit board (FPCB) pre-patterned with interdigital
 347 electrodes (IDEs) with a zoom inset of the interdigital electrodes. (B) Schematic diagram of the
 348 Versatile Acoustofluidic Device (VAD) and a portable control unit, that can drive a cooling fan
 349 and provide radio frequency (RF) signals to drive the two IDTs. The RF signals are amplified by
 350 two 6W power amplifiers (PA1 and PA2). Each IDT is connected to a matching network (MN1
 351 and MN2) for impedance matching. The values of the capacitor (C) and inductor (L) are 68 pF and
 352 470 nH, respectively. The sensing components include two temperature sensors (T1 and T2) and
 353 force-sensitive resistors (FSR1 and FSR2). (C) 3D exploded view of the VAD with an inset
 354 presenting the assembly and components at the localised pressers. (D) The portable control unit
 355 and the VAD with an inset demonstrating the real-life model of the assembled VAD on the
 356 heatsink.



357 (A)

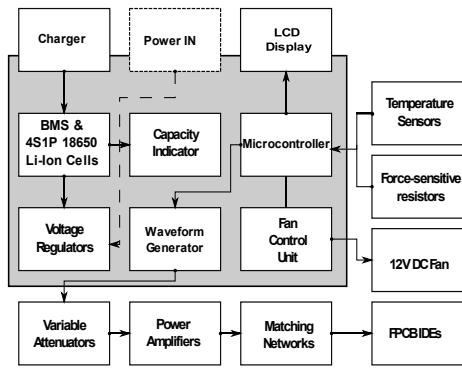


358 (B)



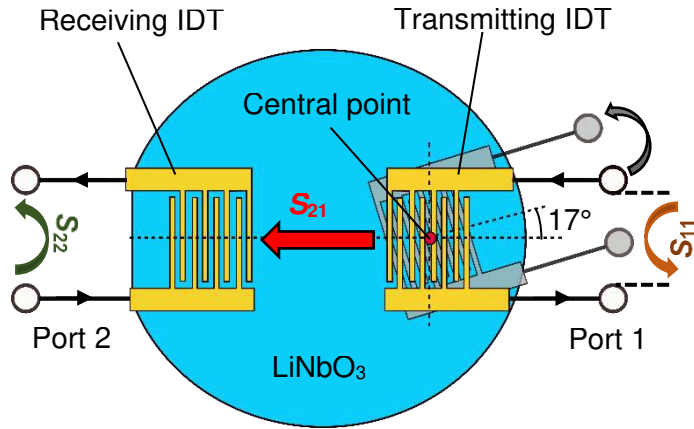
359 (C)

360 **Figure 2.** (A) The development steps of the microchannel using the glass-bottom 3D printed
361 mould. (B) The microchannel presser with its the pressure points and walls highlighted. (C) Real-
362 life models of the glass-bottom 3D printed mould.



363

364 **Figure 3.** The respective block schematic demonstrating all the internal and external components
 365 of the control unit.
 366

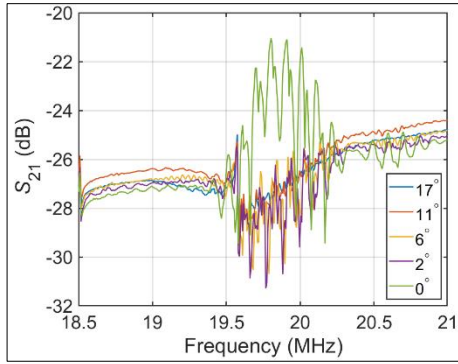


367

368 **Figure 4.** IDT rotation test for investigating the use of the vector network analyser (VNA) to
 369 register the alignment of the IDTs. The transmitting IDT being rotated around its central point,
 370 while the receiving IDT is held fixed.

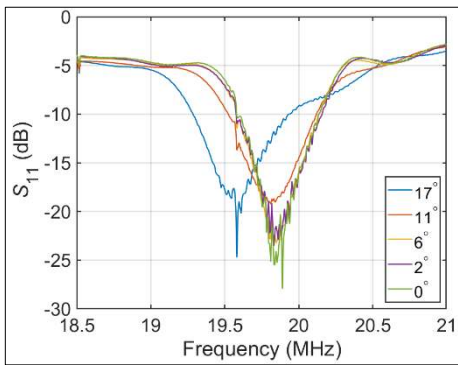
371

(A)



372

(B)



373

Figure 5. S -parameters of the VAD during the rotation of one IDT. (A) Average insertion loss

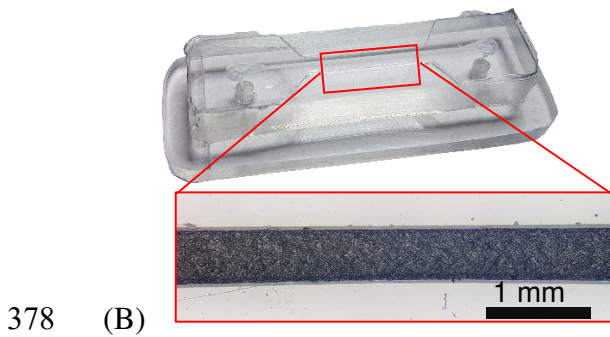
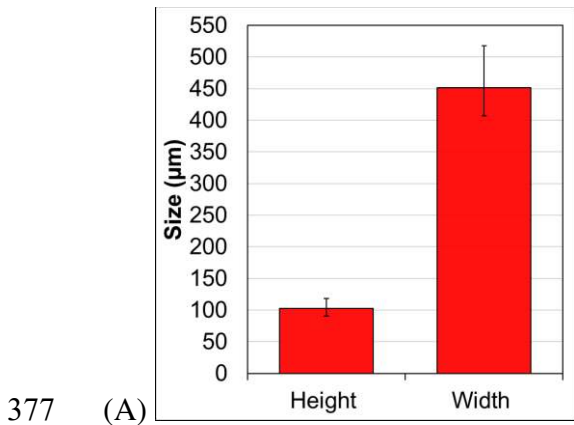
374

(S_{21}) for each different angle during the rotation. (B) Average reflection coefficient (S_{11}) for each

375

different angle during the rotation.

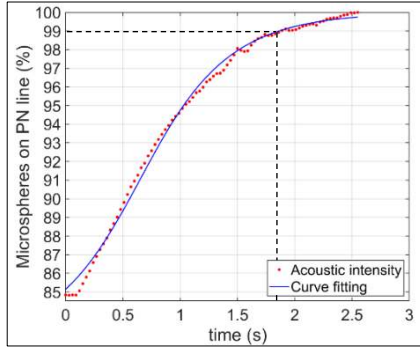
376



379 **Figure 6.** (A) The 3D printed mould's average height and width of $102.8 \pm 11.4 \mu\text{m}$ (Mean \pm SD)
380 and $451.4 \pm 42.6 \mu\text{m}$ (Mean \pm SD), respectively. (B) Real-life model of a $500 \mu\text{m}$ wide
381 microchannel sitting on top of the acrylic presser.

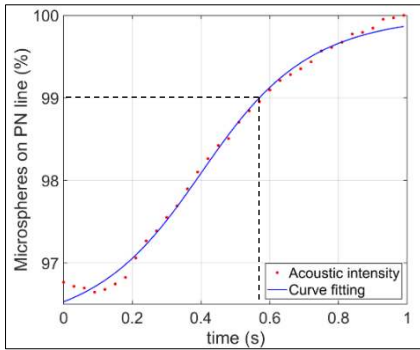
382

(A)



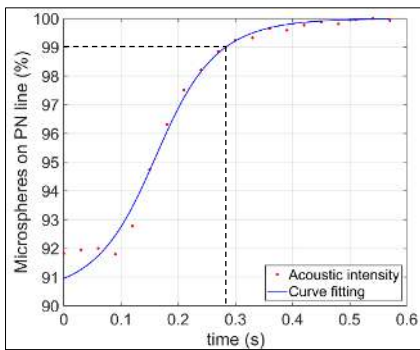
383

(B)



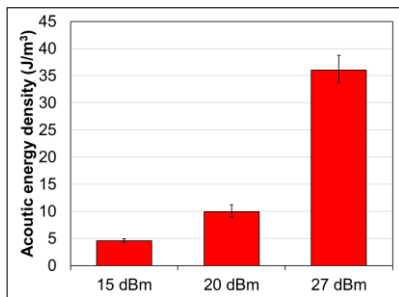
384

(C)

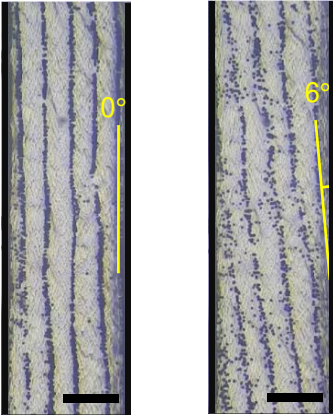


385

(D)



386 **Figure 7.** Acoustic energy density of the VAD with parallel IDTs. (A)-(C) Under the input power
 387 of 15 dBm, 20 dBm, and 27 dBm, the time for 99% of microspheres to reach the PN line is ~1.9,
 388 ~0.6, and ~0.3 sec, respectively. (D) The average acoustic energy densities for the three input
 389 powers are 4.6, 9.9, and 36 J/m³, respectively (n = 3).



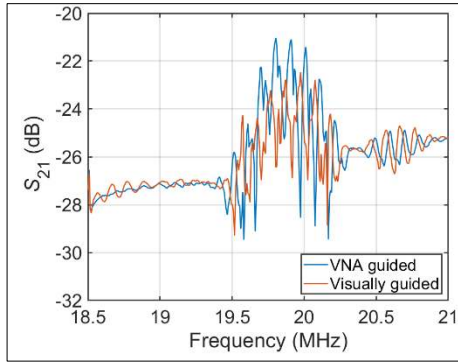
390

391 (A) (B)

392 **Figure 8.** Microscope images showing the reconfigurability of the VAD in setting the PN lines to
393 (A) 0° and (B) 6° . The microspheres are aggregated on the PN lines exhibiting the angle against
394 the wall of the microchannel. (200 μm scale bar)

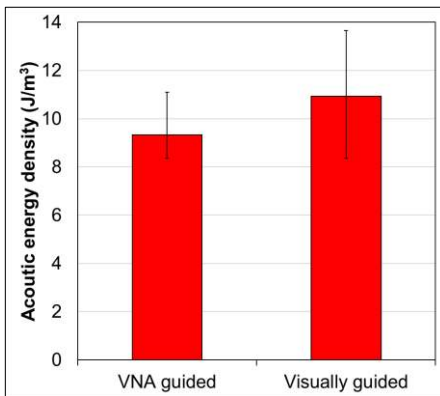
395

(A)



396

(B)

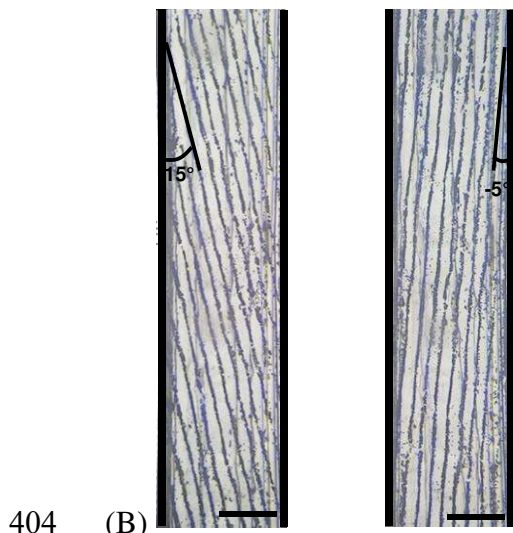
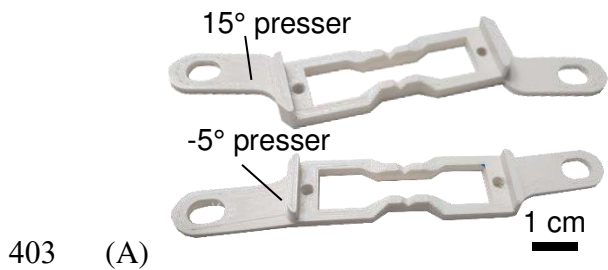


397

(C)



398 **Figure 9.** (A) The S_{21} of the VAD assembled using the VNA and the visually guided assembly of
 399 the two IDTs. ($n = 5$) (B) Acoustic energy density of the VAD constructed by the two assembly
 400 methods, VNA and visually, with an acoustic energy of $9.3 \pm 1.2 J/m^3$ (Mean \pm SD) and $10.9 \pm$
 401 $2.7 J/m^3$ (Mean \pm SD), respectively. ($n = 3$) (C) Microsphere aggregation on the PN lines of the
 402 VAD constructed by visually guided assembly (200 μm scale bar).



405 **Figure 10.** Rotating the microchannel to a set tilted-angle. (A) 3D printed 15° and -5°
406 microchannel pressers. (B) Aggregated microspheres on the PN lines of 15° (left) and -5° (right)
407 angles, in regard to the microchannel wall (450 μm scale bar).

408